Title
Reflective Phase-Contrast for High-Contrast Imaging of van der Waals Heterostructure

Journal
Nano Letters, 23(7)

ISSN
1530-6984

Authors
Kim, Ha-Leem
Wang, Feng

Publication Date
2023-04-12

DOI
10.1021/acs.nanolett.3c00252

Reflective phase-contrast for high-contrast imaging of van der Waals heterostructure

Ha-Leem Kim[a,b], Feng Wang[a,b,*]

[a]Department of Physics, University of California, Berkeley, California 94720, United States

[b]Materials Sciences Division, Lawrence Berkeley National Laboratory, Berkeley, California 94720, United States

*Correspondence to Feng Wang (fengwang76@berkeley.edu)

Abstract

Optical microscopy plays a critical role in the fabrication of two-dimensional (2D) materials, from the first visualization of atomically thin crystals on silicon wafer to controlled stacking of van der Waals heterostructures. An outstanding challenge in conventional microscopy is to visualize transparent 2D layers as well as embedded monolayers in a stacked heterostructure with high optical contrast. Phase-contrast microscopy, first developed by Frits Zernike in the 1930s, leverages the interference effect between specimen scattered light and background light to increase the contrast of transparent specimens. Such phase-contrast microscopy, always in a transmission configuration, revolutionized the study of transparent cellular structures in biology. Here we develop a versatile reflective phase-contrast microscopy for imaging 2D heterostructures. We employ two spatial light modulators to flexibly control the intensity and phase of the illumination and the reflected light. This reflective phase-contrast microscopy achieves unprecedented high contrast for imaging transparent 2D monolayer. It also enables direct observation of 2D monolayers embedded inside a thick heterostructure that are “invisible” in conventional microscopy. The reflective phase-contrast microscopy could be a powerful tool for fabrication and visualization of advanced 2D van der Waals heterostructures.

KEYWORDS:

Phase-contrast microscopy, vanderWaalsheterostructures, spatial light modulators, ring illumination

The successful isolation and manipulation of atomically thin sheets of 2D crystals[1] have ushered in a new era of basic scientific research and technological innovation: atomically thin vdW units with a wide range of properties can now be grown separately and then stacked together to form a new class of materials – vdW-bonded heterostructures. Exploration of novel quantum phenomena in vdW heterostructures has been one of the most exciting fields in condensed matter physics[2-4]. There has been tremendous progress in the study of vdW heterostructures in the last decade, ranging from the observation of atomically thin ferromagnets[5-7] and quantum spin Hall insulators[8-10] to the discovery of correlated insulators[11,12], superconductors[13-16], Chern insulators[17-19], and generalized Wigner crystals[20-24] in vdW moiré superlattices.

Optical microscopy plays a crucial role in the study of vdW heterostructures: it enabled the first identification of 2D monolayers on silicon wafers[25-27] and the fabrication of vdW heterostructures through controlled alignment and mechanical stacking of different layers. Nowadays ever more complicated vdW heterostructures are being created to explore novel quantum phenomena, and it poses significant new challenges for optical microscopy. (1) Some transparent 2D materials, such as hexagonal boron nitride (hBN), has a low optical contrast. As a result, it is very difficult to find monolayer and bilayer hBN in a standard brightfield microscope, although such hBN thin layers can be critical in applications ranging from non-invasive STM spectroscopy[22] to exciton insulator devices[21,28,29]. (2) Although many monolayer materials have reasonable contrast when exfoliated on an optimized SiO2/Si wafer[25,26], they become almost invisible when stacked into a heterostructure in a conventional microscopy. Therefore, it becomes increasingly difficult to track exact position of embedded thin layers as the number of layers in heterostructure increases. This is particularly problematic because the thin layers can shift during the stacking processes, which makes it impossible to achieve designed alignment of different layers. If the invisible layers are on top of the heterostructure, it is possible to visualize the target layers through AFM scanning. However, the scanning range is highly limited and AFM is insensitive to geometry where single atomic layers are embedded in between thick heterostructure.

Here, we develop the reflective phase-contrast microscopy to address these challenges in fabrication of advanced 2D van der Waals heterostructures. Phase-contrast microscopy was first developed by Frits Zernike in the 1930s, which leverages the interference effect between the sample scattered light and the unscattered 0^{th} order light to visualize transparent specimens in biology [30,31]. However, all existing phase-contrast microscopes require transmissive geometry, which is not compatible with the study of 2D heterostructures. We design and implement a versatile reflective phase-contrast microscope that incorporates two spatial light modulators to independently control the illumination and reflection light. We demonstrate the performance of our setup by imaging monolayer and few-layer hBN on various substrates and by visualizing monolayer graphene embedded in thick vdW heterostructures.

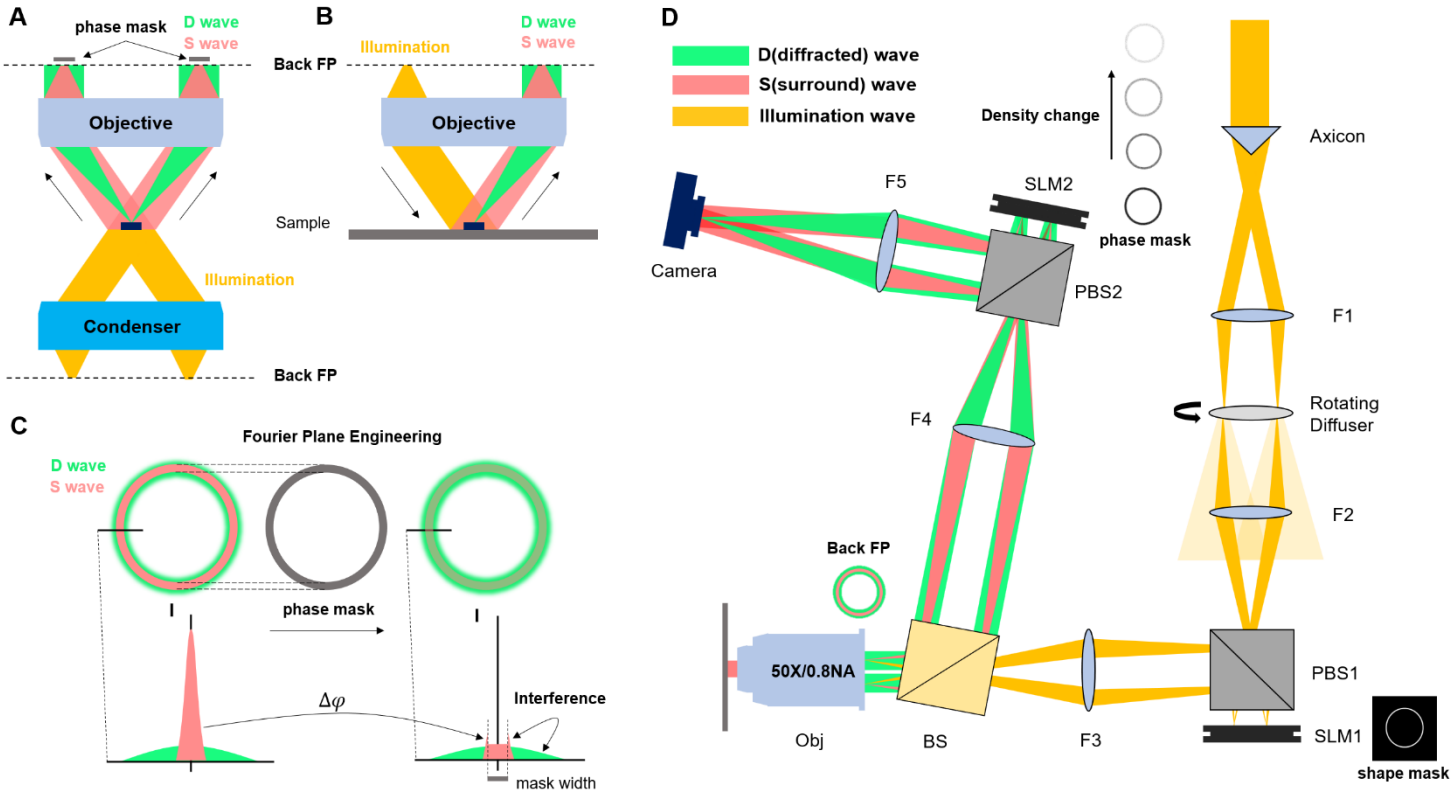

Fig. 1. (A/B) Illustration of the phase-contrast microscopy concept in transmissive/reflective configuration. An incident beam (yellow beam in A, B) is focused at the back focal plane (FP) of the condenser/objective, which forms a plane wave illumination. After illumination, the beam branches into two waves: (1) un-diffracted 0^{th} order S (surrounding) wave and (2) D (diffracted) wave, which scatters in many directions. S wave intact from the specimen focus as a bright ring on the back FP (red beam in A, B). However, D wave penetrates the back FP at various locations around the ring focus formed by S wave (green beam in A, B). D wave cover the whole back FP in reality, but only part of D wave is drawn in the figure. (C) By locating the phase mask on the Fourier plane, the amplitude/phase of the S wave can be selectively modulated to produce an optimal interference effect between S and D waves. (D) Delineate optical setup of our reflective phase-contrast system. Laser light combined with an Axicon and an imaging lens (F1) were used to achieve high throughput ring illumination. Incoherent illumination was created by placing a rotating diffuser at the lens focus of F1. The ring focus created by the Axicon-lens is not ideal and has a halo-like background. Lens F2 re-images incoherent ring focus onto SLM1, where a shape mask was implemented to create a clean, narrow background-free ring focus (see insert 'shape mask'). Lens F3 re-images the perfect ring focus onto the back FP of the objective for illumination. After beamsplitter (BS), back FP of was re-imaged onto the second SLM (SLM2) via lens F4. A highly tunable ring phase mask was created by SLM2 to modulate the phase and amplitude of the S wave (see insert 'phase mask'). The beamsplitter was intentionally tilted to avoid multiple reflections from the objective.

Fig. 1A (B) illustrates the concept of the phase contrast microscopy in transmission (reflection) configuration. The incident beam is focused at the back focal plane of the condenser (objective), which forms a plane wave illumination on the sample. After transmission

(reflection), the imaging beam can be divided into two waves: (1) an un-diffracted 0^{th} order surrounding wave (S wave) that passes through the specimen but does not interact with it, and (2) a diffracted wave (D wave) which get scattered to many different directions[32]. Both S and D waves are collected by the objective. There interference at the imaging plane ($\tilde{E}_{total} = \tilde{E}_S + \tilde{E}_D$) gives rise to the sample image observed in a CCD camera. For samples with weak contrast, the diffracted wave $\tilde{E}_D$ is small and often out of phase with $\tilde{E}_S$. The phase-contrast microscope selectively modulates the amplitude and relative phase of $\tilde{E}_S$ to optimize interference between S and D waves. This selective modulation is achieved at the Fourier plane of the image, e.g. the back focal plane (FP) of the objective, where the S wave (red beam in **Fig. 1A, B**) and the D wave (green beam in **Fig. 1A, B**) are spatially separated. D wave cover the whole back FP in reality, but only part of the D wave is drawn in the figure.

In practice a ring-shaped illumination is used in a conventional transmissive phase-contrast microscope, which is generated by an annulus at the back FP of the condenser. Such ring illumination increases the resolution of an image compared to point illumination by enhancing an effective numerical aperture of the illumination beam. Afterward, a ring-shaped phase plate located on the objective back FP selectively reduces the amplitude of $\tilde{E}_S$ and shifts its relative phase to create maximum contrast in the image (see **Fig. 1C**). For reflective geometry, however, the objective is used for both illumination and collection. Thus, it is impossible to adopt the conventional transmissive design; otherwise, a phase plate on the back FP will affect the illumination beam. To address this challenge, we re-image the objective back FP on two Spatial Light Modulators (SLMs) to achieve separate and flexible control of the illumination and the reflected beams.

Fig. 1D shows the optical setup of our reflective phase-contrast microscope. We use a laser light source combined with an Axicon and an imaging lens (F1) to achieve a ring-shaped beam with high brightness. For optical imaging, an incoherent illumination is desirable to avoid coherent artifacts that can strongly degrade the image quality. Such an incoherent beam is achieved by introducing a rotating diffuser at the lens focus of F1. However, the ring pattern created by the Axicon-lens pair and the diffuser is not ideal and has a strong halo-like background. To generate a clean ring illumination with minimum background light, we use a lens (F2) to image the ring-shaped incoherent light from the rotating diffuser onto the first SLM (SLM1). A ring-shaped mask pattern is implemented in the SLM1 to create the optimal ring illumination that is clean, bright, narrow, and incoherent (see insert 'shape mask' on **Fig. 1D** and **Supplementary Note. 1**). This optimized ring illumination is further re-imaged by the lens F3 to the back FP of the objective. After illuminating the sample, the diffracted D waves surround S waves on the objective back FP. After the beamsplitter (BS), we re-image this back FP onto the second SLM (SLM2). By feeding a grayscale ring image on SLM2, we can selectively and flexibly modulate both the phase and amplitude of the S wave $\tilde{E}_S$ (see insert 'phase mask' on **Fig. 1D**). To get a high contrast image, the alignment of the phase mask is critical[32]. The radius, width, and position of the amplitude-phase mask on SLM2 were fine-tuned by imaging the diffraction plane *in-situ*. The beamsplitter behind the objective was intentionally tilted to avoid multiple reflections from the objective, which otherwise created a ring artifact on the final image.

We use liquid-crystal-on-silicon (LCOS) SLMs from commercial Sony projectors for phase and amplitude control. The principal axis of the liquid crystal layer is at 45 degrees, which creates an electrically tunable phase delay $\Delta\theta$ between the electrical field along the $\frac{\hat{x}+\hat{y}}{2}$

and $\frac{\hat{x}-\hat{y}}{2}$ axis. For a linearly polarized incident light $\tilde{\vec{E}}_i = E_0\hat{x} = E_0(\frac{\hat{x}+\hat{y}}{2} + \frac{\hat{x}-\hat{y}}{2})$, the reflected light from the SLM is $\tilde{\vec{E}}_i = E_0\hat{x} = E_0(\frac{\hat{x}+\hat{y}}{2} + \frac{\hat{x}-\hat{y}}{2}e^{i\Delta\theta}) = E_0[e^{\frac{i\Delta\theta}{2}}\cos\left(\frac{\Delta\theta}{2}\right)\hat{x} + e^{i\left(\frac{\Delta\theta-\pi}{2}\right)}\sin\left(\frac{\Delta\theta}{2}\right)\hat{y}]$. The output light after the polarizing beamsplitter (PSB) is therefore $\tilde{\vec{E}}_o = E_0 e^{i\left(\frac{\Delta\theta-\pi}{2}\right)}\sin\left(\frac{\Delta\theta}{2}\right)\hat{y}$. Therefore, we can create an effective phase shift $\Delta\varphi = \frac{\Delta\theta-\pi}{2}$ and amplitude reduction of $\sin\left(\frac{\Delta\theta}{2}\right)$ at individual pixel level by varying the greyscale intensity from 0 ($\Delta\theta = 0$) to 255 ($\Delta\theta = \pi$). In addition, the amplitude can independently be controlled by varying the density, ρ, of non-zero pixels inside the ring mask on the SLM (see **Supplementary Note. 2**).

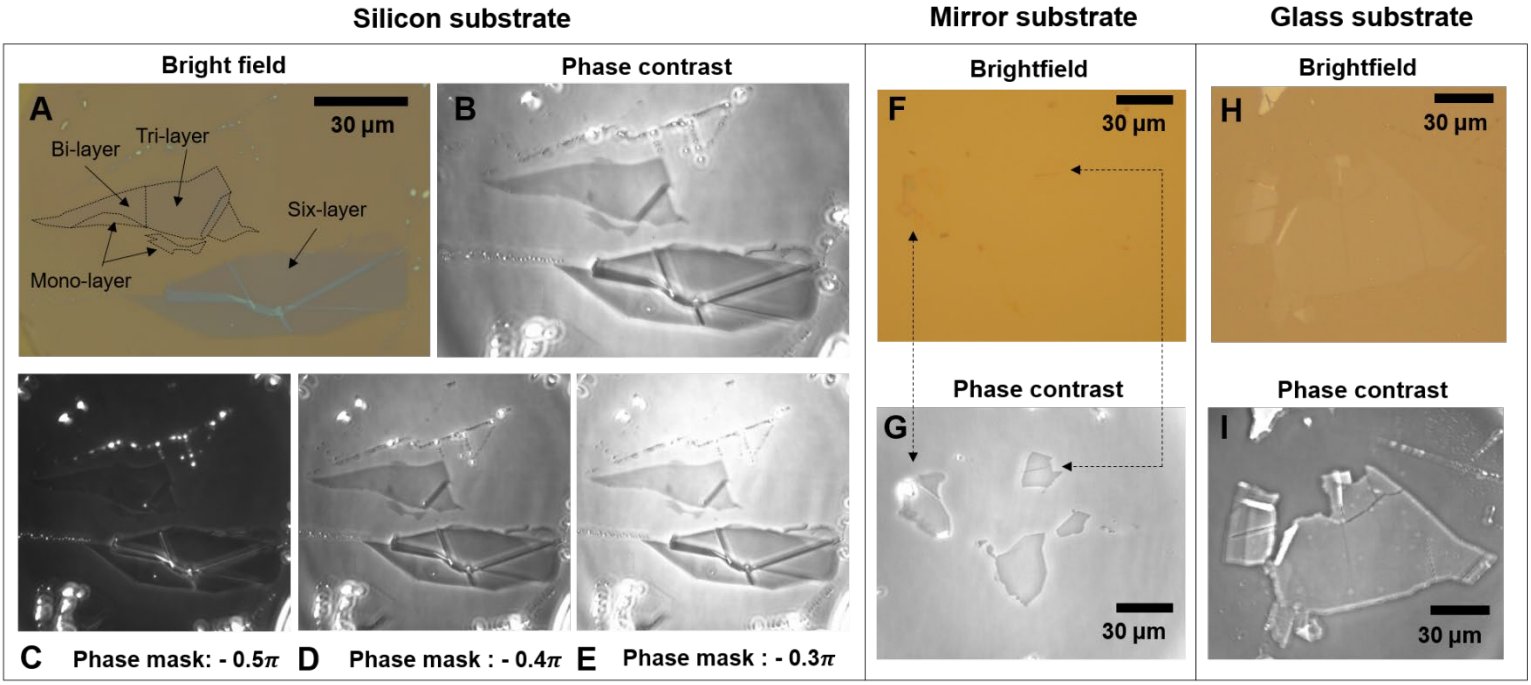

Fig. 2. (A) Brightfield and (B) 650 nm phase-contrast images of the mono/bi/tri/six layers hBN exfoliated on 90 nm SiO2/Si wafer. Monolayer hBN is hardly visible under brightfield imaging. Under the phase-contrast microscope, the monolayer gains strong visibility. Same flakes were imaged varying phase-mask: (C) -0.5π, (D) -0.4π, (E) -0.3π. Monolayer contrast reaches up to 13% for -0.4π phase mask. To further test the performance of the microscope, hBN was exfoliated directly on a mirror substrate and imaged using (F) brightfield and (G) phase-contrast microscope. Due to the reduced local field factor, exfoliated hBN is completely invisible under the brightfield microscope. Through phase-modulation, all hidden flakes on the mirror are discernable. Moreover, hBN was directly exfoliated on a slide glass to simulate the cases when a device is supported by a transparent PDMS stamp or transparent substrates. Brightfield imaging barely gives contrast (H). However, contrast can be much increased through phase modulation (I). Though transparent, glass reflects a few percent of the incident light and phase modulation is still applicable. Even cracks and small dust particles on the flakes were resolved.

We first test the reflective phase-contrast microscope on a few-layer hBN sample. **Fig. 2A and B** compare images taken from a standard brightfield and the red (650 nm) laser phase-contrast microscope for mono/bi/tri/six layers hBN exfoliated on a 90 nm SiO2/Si wafer. Mono/bilayers hBN are hardly visible under the brightfield microscope. However, optical contrast gets strongly enhanced in the phase-contrast microscope. **Figure 2C, D, and E** display the phase-contrast images for phase shifts $\Delta\varphi = -0.5\pi$, -0.4π and -0.3π with full density ring mask, respectively. For $\Delta\varphi = -0.5\pi$ and full density phase mask (filled black ring), SLM2-PBS almost completely blocks the S waves (limited by the extinction ratio of LCD). This corresponds to a dark-field microscopy configuration. Monolayer contrast reaches up to 13% for -0.4π phase mask.

The phase-contrast microscope can visualize not only thin hBN on a SiO2/Si substrate, but also on transparent glass substrates and highly reflective mirror substrates. Depending on a substrate local field factor, the amplitude of D waves is different, which is why optimized the SiO2/Si substrate can give better contrast for atomically thin layers[25,26]. However, it is sometimes necessary to exfoliate 2D materials on substrates different from the SiO2/Si substrate, which can make it difficult to observe the exfoliated 2D monolayers. For example, the hBN flakes completely lose contrast on the mirror substrate under the brightfield microscope (**Fig. 2F**). However, in the phase-contrast image, every layer on the mirror substrate becomes visible. It demonstrates the high performance of our phase-contrast setup (**Fig. 2G**). Thin hBN layers exfoliated on transparent cover glass were also examined using the phase-contrast microscope. The transparent glass substrate reflects a few percent of the incident light and phase modulation is still applicable. Under the brightfield microscope (**Fig. 2H**), thin hBN flakes on glass are hardly visible. In comparison, we can easily observe the thin hBN flakes on glass in the phase-contrast microscope (**Fig. 2I**). Even cracks and small dust particles on the flakes can be readily resolved.

Next, we quantitatively characterize the optical contrast for green (520 nm) lasers phase-contrast microscope as a function of the two phase mask parameters: the density ρ and phase shift $\Delta\varphi$. We use the monolayer hBN on the 90nm SiO2/Si substrate as the test samples. **Fig. 3A** displays the experimental data. Along the $\rho = 0$ or $\Delta\varphi = 0$ axis, parameters correspond to a brightfield image with no phase mask. Without any phase/amplitude modulation, the contrast of monolayer hBN is 0.8%, near zero. The maximum contrast occurs along the $\rho = 1$ axis (full ring), and the absolute value reaches 18% at $\Delta\varphi \sim -0.42\pi$. The lobe feature in the contrast map (black dashed line in **Fig. 3A**) is due to competing two factors for achieving optimal interference effect: trying to make maximum phase difference π between S and D waves versus keeping the amplitude of S wave finite.

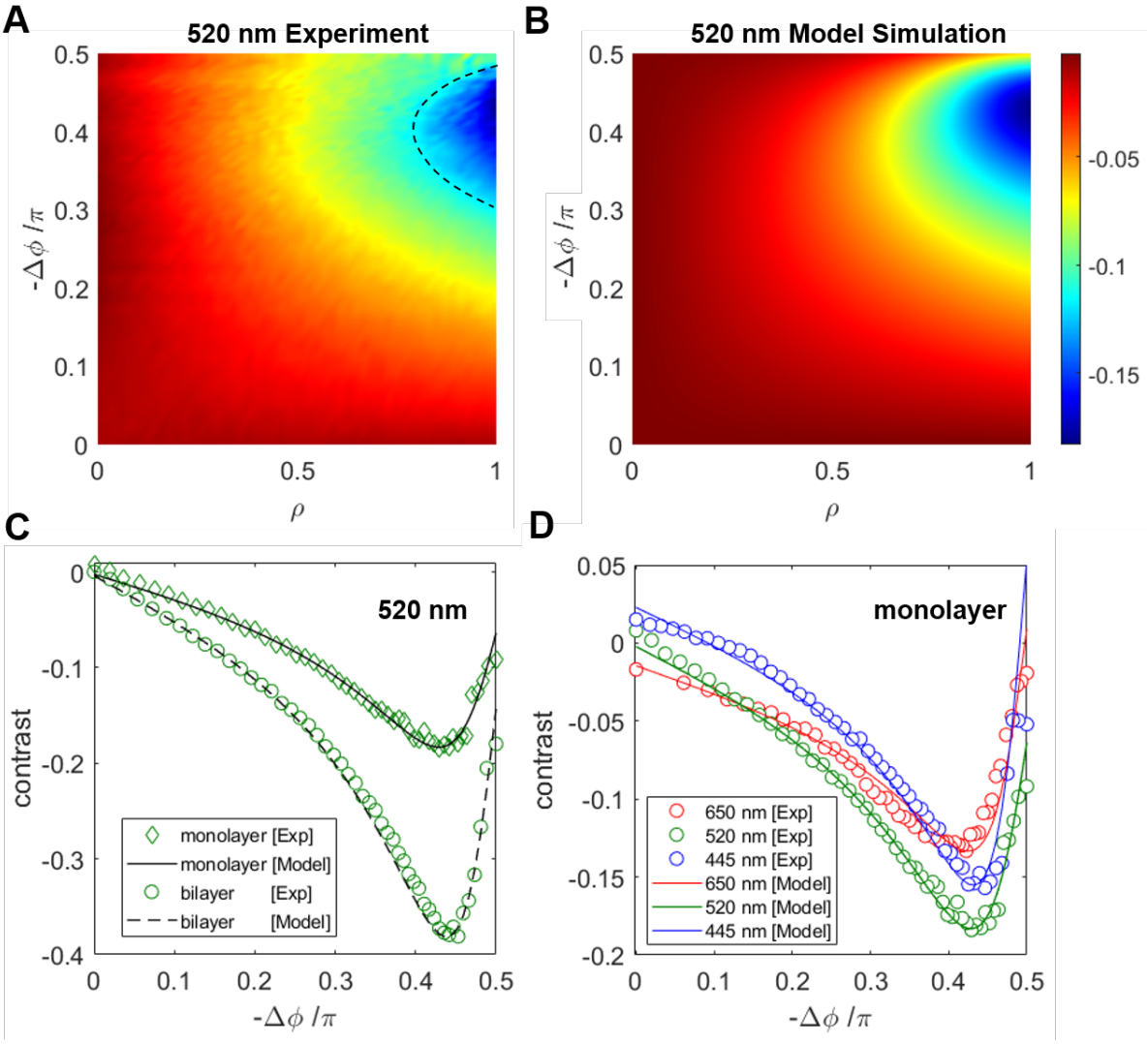

Fig. 3. (A) Optical contrast scan of monolayer hBN on 90nm SiO2/Si wafer varying the phase mask parameters: the density ρ and phase shift Δφ. 520nm green laser was used. Along the $\rho = 0$ or $\Delta\varphi = 0$ axis, parameters correspond to a brightfield image (no phase modulation) and the contrast of monolayer hBN is 0.8%. The maximum contrast reaches 18% at mask parameter $\Delta\varphi \sim -0.42\pi$, $\rho = 1$. The lobe feature in the contrast map (black dashed line in A) is due to competing two factors for achieving optimal interference: trying to make maximum phase difference π between S and D waves versus keeping the amplitude of S wave finite. (B) The behavior of the phase mask for the monolayer was simulated and compared with the experimental data (see main text for detailed modeling). Simulation well predicts position and magnitude of the lobe feature with high accuracy. (C) Contrast for monolayer and bilayer hBN along the $\rho = 1$ axis was compared. Maximal contrast for both layers occurs on the same mask parameter $\Delta\varphi \sim -0.42\pi$, and magnitude increased twofold for the bilayer. Simulation correctly explains bilayer contrast data as well. (D) Experimental data and model simulation were summarized for 650nm, 520nm and 445nm lasers along the ρ=1 axis. For a standard brightfield image ($\Delta\varphi$=0), contrast is higher for the blue/red laser, and green is lowest. However, the maximum contrast achievable by the phase-contrast microscope is highest for green laser. This is consistent with model and can be understood intuitively. The 520nm brightfield imaging has the lowest contrast since S and D waves are most out of phase (0.49π).

However, the scattering amplitude (0.045) is the highest among the three wavelengths. Thus, contrast at the optimal interference condition should be the highest. For reflective geometry, Rayleigh elastic scattering amplitude depends on the local field factor. Hence, the highest frequency, blue, does not necessarily correspond to the highest scattering amplitude.

The experimental data can be well described by our model simulation. The electric field of the S and D waves are described by

$$\tilde{E}_D = \epsilon e^{i\Delta\varphi_0}$$

$$\tilde{E}_S = \left(\sin\left(\Delta\varphi + \frac{\pi}{2}\right) e^{i\Delta\varphi}\rho + (1-\rho)\right) \times (1 - r_A) + r_A$$

Here ϵ is the relative strength of D waves (compared to S waves), $\Delta\varphi_0$ is a phase shift of D waves relative to S waves as it interacts with the sample, $\Delta\varphi$ is a phase change produced by the SLM on a pixel level and $\rho \in [0,1]$ is the pixel density of the phase mask. Additional parameter $r_A \ll 0.1$ was included because the focused S waves on the Fourier plane have a finite width, and the phase mask only modulates the part of the region leaving r_A portion of S waves unaffected. Field intensities at sample position and nearby background region on an image plane are then given by $I_{sample} = \left|\tilde{E}_S + \tilde{E}_D\right|^2 + e_b$ and $I_{background} = \left|\tilde{E}_S\right|^2 + e_b + e_{offset}$ where $e_b \ll 0.1$ is an environmental background and $e_{offset} \ll 0.1$ is a factor accounting for the spatial inhomogeneity of background light. Intrinsic parameters $\epsilon = 0.45$, $\Delta\varphi_0 = 0.49\pi$ for monolayer hBN were determined from the thin film model[25,26] (see **Supplementary Note. 3**). Contrasts, $(I_{sample} - I_{background})/I_{background}$, were calculated where corresponding maps are shown in **Fig. 3B**. Calculation well predicts lobe feature, and maximum contrast occurs along the $\rho = 1$ axis at $\Delta\varphi \sim -0.42\pi$ agreeing with the experimental data. Calculation even predicts the contrast magnitude with high accuracy. However, experimental data is broadened along the ρ axis compared to the model. This is because, in model simulation, perfect coherence within the width of the S wave ring focus was assumed, yet the rotating diffuser reduces coherence in the experiment. Thus, broadening along the ρ axis is expected. Contrast for monolayer and bilayer hBN along the $\rho = 1$ axis was compared (**Fig. 3C**). Maximal contrast for both layers occurs on the same mask parameter, and magnitude increased twofold for the bilayer. Bilayer scattering amplitude $\epsilon = 0.9$ is twice that of monolayer and scattering phase shift $\Delta\varphi_0 = 0.49\pi$ is same as monolayer. With the parameters, model simulation correctly explains bilayer contrast data.

Further, we measured contrast along the $\rho = 1$ axis varying laser wavelength. Experimental data and model simulation for 650nm, 520nm, and 445nm lasers are summarized in **Fig. 3D**. For model simulation, intrinsic parameters $\epsilon = 0.031/0.045/0.043$, and $\Delta\varphi_0 = 0.58\pi/0.49\pi/0.42\pi$ were computed for each corresponding wavelength from the thin film model[25,26]. For normal brightfield image ($\Delta\varphi$=0), contrast is higher for blue/red laser, and green is lowest. However, the maximum contrast achievable by the phase-contrast microscope is highest for green laser (~18%). This is consistent with model simulation and can be understood intuitively. The 520nm brightfield image without any phase mask has the lowest contrast since S and D waves are most out of phase ($\Delta\varphi_0 = 0.49\pi$). However, the scattering amplitude $\epsilon = 0.045$ is the highest among the three wavelengths. Thus, contrast at the optimal interference condition should be the highest. For reflective geometry, Rayleigh elastic scattering amplitude depends on the local field factor. Hence, the highest frequency, blue, does not necessarily

correspond to the highest scattering amplitude and scattering amplitude varies in terms of the SiO2 thickness.

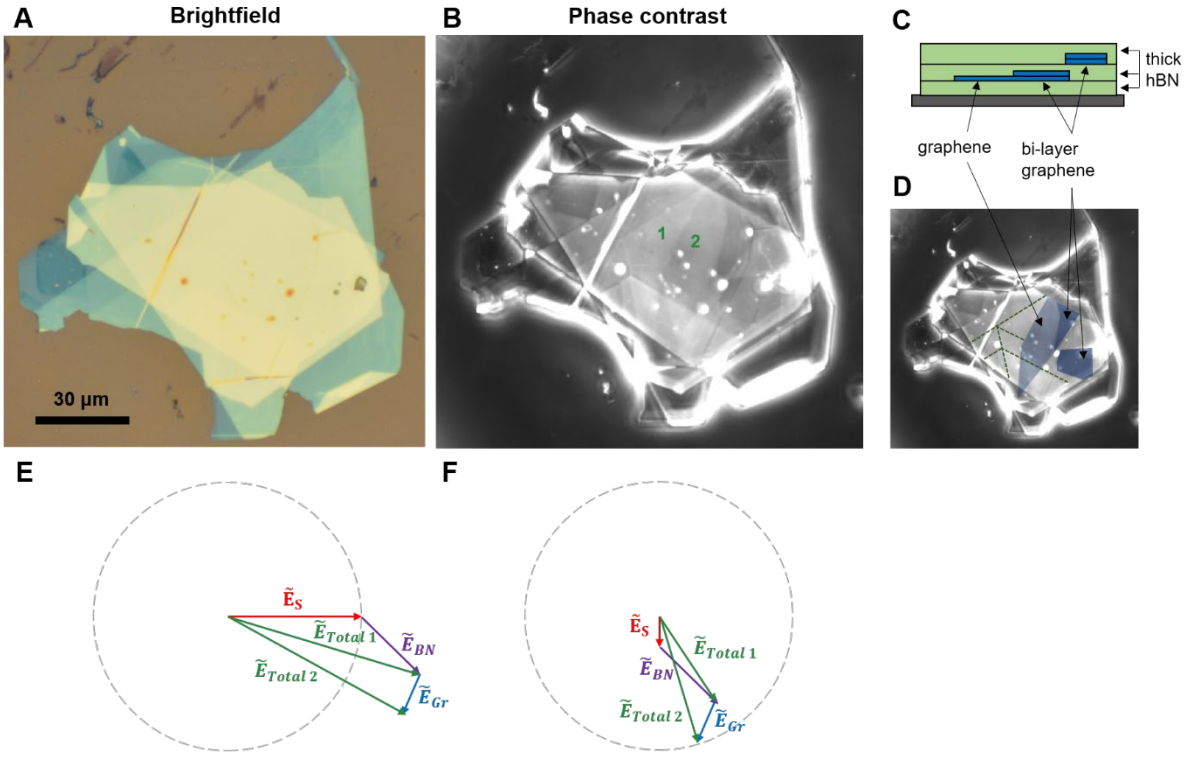

Fig. 4. (A) Brightfield and (B) 650nm phase-contrast image on hBN-Gr-hBN-Gr-hBN heterostructure. (C) Mono/bilayers graphene are embedded in thick hBN layers (~35 nm for each). All graphene layers (blue region in D) invisible under the standard brightfield microscope are discernible through the phase-contrast modulation. Even inhomogeneity of thick hBN layers inside the overlapping area can be distinguished (green dashed lines in D). For phase-contrast image, the boundaries of the heterostructure or any bubbles inside it get brighter than the bulk part due to the relative enhancement of high spatial frequency information. E, F explains the principle of phase-contrast technic on heterostructure device. In region 1 of B, only thick overlapped hBN is present, and the total electric field at the point is $\tilde{E}_{Total\,1} = \tilde{E}_S + \tilde{E}_{BN}$, where $\tilde{E}_S$ is unscattered light and $\tilde{E}_{BN}$is scattered light from hBN. In region 2 of B, embedded graphene is located and the total field is $\tilde{E}_{Total\,2} = \tilde{E}_S + \tilde{E}_{BN} + \tilde{E}_{Gr}$ where $\tilde{E}_{Gr}$ is scattered light from graphene. In standard brightfield imaging, $\tilde{E}_{Total\,1}$ and $\tilde{E}_{Total\,2}$ have the same amplitude, and the graphene is invisible (E). However, by modulating phase of $\tilde{E}_S$ and reducing its amplitude, it is possible to achieve amplitude differences between two total waves (F).

The developed phase-contrast setup becomes most powerful when it comes to visualizing transparent embedded thin layers inside a thick heterostructure device. We demonstrate that the phase-contrast technique can give clear contrast for invisible graphene embedded in thick hBN, a typical complication when making high functionality optical devices. **Fig. 4A** and **B** correspond to images taken from a brightfield and red (650nm) laser phase-contrast microscope for BN-Gr-BN-Gr-BN heterostructure (see **Fig. 4C, D** for device structure). Mono/bilayers graphene are embedded in thick hBN layers (~35 nm for each). Under the brightfield microscope, all graphene layer becomes completely invisible. However, one can distinguish every hidden graphene structure via the phase/amplitude modulation (blue

region in **Fig. 4D**). Even the inhomogeneities of thick hBN on the overlapping area can be discerned (green dashed line in **Fig. 4D**). For phase-contrast image, the boundaries of the heterostructure or any bubbles inside it get brighter than the bulk part. This is because the D wave's high/low spatial frequency components are situated further/closer to the S waves. Thus, the phase mask not only reduces the amplitude of the S wave but also increases the relative strength of high spatial frequency information of the heterostructure.

The behavior of phase-contrast modulation on a heterostructure device is more complex compared to a single flake. For single flake imaging on a silicon wafer, the camera detects contrast between flake position and nearby substrate region. Thus, the local intensity of the S wave, $\tilde{E}_S$, and total wave, $\tilde{E}_S + \tilde{E}_D$, are being compared. However, for heterostructure imaging, contrast is measured between two different locations "on" a device. In region 1 of **Fig. 4B**, only thick overlapped hBN is present, and the total electric field at the point is $\tilde{E}_{Total\,1} = \tilde{E}_S + \tilde{E}_{BN}$, where $\tilde{E}_{BN}$ is diffracted light from hBN. In region 2 of **Fig. 4B**, embedded graphene is present, and the total field is $\tilde{E}_{Total\,2} = \tilde{E}_S + \tilde{E}_{BN} + \tilde{E}_{Gr}$ where $\tilde{E}_{Gr}$ is diffracted light from graphene. In standard brightfield imaging, $\tilde{E}_{Total\,1}$ and $\tilde{E}_{Total\,2}$ has the same amplitude, and the graphene is invisible (see vector diagram **Fig. 4E**). However, by modulating phase of the S wave and reducing its amplitude, it is possible to achieve amplitude differences between two total waves (see vector diagram **Fig. 4F**). Depending on the wavelength, the local field factor and phase shift are different. Thus, we can choose the laser wavelength that provides the highest optical contrast in each heterostructure sample. For current geometry, red laser phase-contrast shows the highest contrast for visualizing graphene layers.

In conclusion, we developed the reflective phase-contrast microscope to visualize a few atomic layers with a superb contrast level (~18% for monolayer hBN) and to discern transparent 2D layers embedded inside a thick heterostructure. Its unique capability can greatly facilitate the fabrication of sophisticated van der Waals heterostructures to realize novel quantum phenomena.

Supporting Information

Shaping perfect ring illumination, Tuning phase mask parameters, Calculating scattering phase-shift/amplitude of hBN using a thin film model

Acknowledgements

The work is supported by the Director, Office of Science, Office of Basic Energy Sciences, Materials Sciences and Engineering Division of the US Department of Energy under contract number DE-AC02-05CH11231 (vdW heterostructure Program KCWF16). H.L. thanks Sixuan Li and Nathan Song for providing testing samples, monolayer flakes for phase-contrast imaging.

Reference

1 Liu, Y. *et al.* Van der Waals heterostructures and devices. *Nature Reviews Materials* **1**, 16042 (2016).

https://doi.org:10.1038/natrevmats.2016.42
2 Geim, A. K. & Novoselov, K. S. The rise of graphene. *Nature Materials* **6**, 183-191 (2007). https://doi.org:10.1038/nmat1849
3 Regan, E. C. *et al.* Emerging exciton physics in transition metal dichalcogenide heterobilayers. *Nature Reviews Materials* **7**, 778–795 (2022). https://doi.org:10.1038/s41578-022-00440-1
4 Das, S., Robinson, J. A., Dubey, M., Terrones, H. & Terrones, M. Beyond Graphene: Progress in Novel Two-Dimensional Materials and van der Waals Solids. *Annual Review of Materials Research* **45**, 1-27 (2015). https://doi.org:10.1146/annurev-matsci-070214-021034
5 Fei, Z. *et al.* Two-dimensional itinerant ferromagnetism in atomically thin Fe3GeTe2. *Nature Materials* **17**, 778-782 (2018). https://doi.org:10.1038/s41563-018-0149-7
6 Gong, C. *et al.* Discovery of intrinsic ferromagnetism in two-dimensional van der Waals crystals. *Nature* **546**, 265-269 (2017). https://doi.org:10.1038/nature22060
7 Huang, B. *et al.* Layer-dependent ferromagnetism in a van der Waals crystal down to the monolayer limit. *Nature* **546**, 270-273 (2017). https://doi.org:10.1038/nature22391
8 Tang, S. *et al.* Quantum spin Hall state in monolayer 1T'-WTe2. *Nature Physics* **13**, 683-687 (2017). https://doi.org:10.1038/nphys4174
9 Wu, S. *et al.* Observation of the quantum spin Hall effect up to 100 kelvin in a monolayer crystal. *Science* **359**, 76-79 (2018). https://doi.org:10.1126/science.aan6003
10 Lodge, M. S., Yang, S. A., Mukherjee, S. & Weber, B. Atomically Thin Quantum Spin Hall Insulators. *Advanced Materials* **33**, 2008029 (2021). https://doi.org:https://doi.org/10.1002/adma.202008029
11 Wang, L. *et al.* Correlated electronic phases in twisted bilayer transition metal dichalcogenides. *Nature Materials* **19**, 861-866 (2020). https://doi.org:10.1038/s41563-020-0708-6
12 Huang, X. *et al.* Correlated insulating states at fractional fillings of the WS2/WSe2 moiré lattice. *Nature Physics* **17**, 715-719 (2021). https://doi.org:10.1038/s41567-021-01171-w
13 Cao, Y. *et al.* Unconventional superconductivity in magic-angle graphene superlattices. *Nature* **556**, 43-50 (2018). https://doi.org:10.1038/nature26160
14 Oh, M. *et al.* Evidence for unconventional superconductivity in twisted bilayer graphene. *Nature* **600**, 240-245 (2021). https://doi.org:10.1038/s41586-021-04121-x
15 Lu, X. *et al.* Superconductors, orbital magnets and correlated states in magic-angle bilayer graphene. *Nature* **574**, 653-657 (2019). https://doi.org:10.1038/s41586-019-1695-0
16 Zhou, H., Xie, T., Taniguchi, T., Watanabe, K. & Young, A. F. Superconductivity in rhombohedral trilayer graphene. *Nature* **598**, 434-438 (2021). https://doi.org:10.1038/s41586-021-03926-0
17 Chen, G. *et al.* Tunable correlated Chern insulator and ferromagnetism in a moiré superlattice. *Nature* **579**, 56-61 (2020). https://doi.org:10.1038/s41586-020-2049-7
18 Xie, Y. *et al.* Fractional Chern insulators in magic-angle twisted bilayer graphene. *Nature* **600**, 439-443 (2021). https://doi.org:10.1038/s41586-021-04002-3
19 Spanton Eric, M. *et al.* Observation of fractional Chern insulators in a van der Waals heterostructure. *Science* **360**, 62-66 (2018). https://doi.org:10.1126/science.aan8458
20 Regan, E. C. *et al.* Mott and generalized Wigner crystal states in WSe2/WS2 moiré superlattices. *Nature* **579**, 359-363 (2020). https://doi.org:10.1038/s41586-020-2092-4
21 Zhang, Z. *et al.* Correlated interlayer exciton insulator in heterostructures of monolayer WSe2 and moiré WS2/WSe2. *Nature Physics* **18**, 1214-1220 (2022). https://doi.org:10.1038/s41567-022-01702-z
22 Li, H. *et al.* Imaging two-dimensional generalized Wigner crystals. *Nature* **597**, 650-654 (2021). https://doi.org:10.1038/s41586-021-03874-9
23 Jin, C. *et al.* Stripe phases in WSe2/WS2 moiré superlattices. *Nature Materials* **20**, 940-944 (2021). https://doi.org:10.1038/s41563-021-00959-8
24 Smoleński, T. *et al.* Signatures of Wigner crystal of electrons in a monolayer semiconductor. *Nature* **595**, 53-57 (2021). https://doi.org:10.1038/s41586-021-03590-4
25 Blake, P. *et al.* Making graphene visible. *Applied Physics Letters* **91,** 063124 (2007). https://doi.org:10.1063/1.2768624
26 Gorbachev, R. V. *et al.* Hunting for monolayer boron nitride: optical and Raman signatures. *Small* **7**, 465-468 (2011). https://doi.org:10.1002/smll.201001628
27 Jessen, B. S. *et al.* Quantitative optical mapping of two-dimensional materials. *Scientific Reports* **8**, 6381 (2018). https://doi.org:10.1038/s41598-018-23922-1
28 Gu, J. *et al.* Dipolar excitonic insulator in a moiré lattice. *Nature Physics* **18**, 395-400 (2022). https://doi.org:10.1038/s41567-022-01532-z
29 Li, J. I. A., Taniguchi, T., Watanabe, K., Hone, J. & Dean, C. R. Excitonic superfluid phase in double bilayer graphene. *Nature Physics* **13**, 751-755 (2017). https://doi.org:10.1038/nphys4140
30 Zernike, F. Das Phasenkontrastverfahren bei der mikroskopischen Beobachtung. *Z. Techn. Physik.* **16**,

454-457 (1935).
31 Zernike, F. How I discovered phase contrast. *Science* **121**, 345-349 (1955). https://doi.org:10.1126/science.121.3141.345
32 Douglas B. Murphy, M. W. D. *Fundamentals of Light Microscopy and Electronic Imaging,* 2nd ed.; John Wiley and Sons: New Jersey, 2012.